Results in Engineering 30 (2026) 110037

Contents lists available at ScienceDirect

Results in Engineering

journal homepage: www.sciencedirect.com/journal/results-in-engineering

Research paper

Phenology-preserving temporal reconstruction of satellite-derived NDVI via morphological operations for unsupervised vegetation clustering

Hooman Hosseini [a], Brigitte Kaufmann [b,c], Oliver Hensel [a,*], Abozar Nasirahmadi [a,d]

[a] Department of Agricultural and Biosystems Engineering, University of Kassel, Witzenhausen 37213, Germany
[b] German Institute for Tropical and Subtropical Agriculture (DITSL), Steinstrasse 19, 37213 Witzenhausen, Germany
[c] Social Ecology of Tropical and Subtropical Land-Use Systems, Institute of Agricultural Sciences in the Tropics (Hans-Ruthenberg-Institute), University of Hohenheim, 70599 Stuttgart, Germany
[d] Department of Energy and Technology, Swedish University of Agricultural Sciences, Box 7032, Uppsala 75007, Sweden

ARTICLE INFO

Keywords:
Unsupervised vegetation classification
Vegetation index time series signal restoration
Morphological filtering
Cloud-affected satellite data
Rangeland monitoring

ABSTRACT

Cloud contamination remains a major challenge in the analysis of satellite-derived Normalized Difference Vegetation Index (NDVI) time series, particularly in dryland and semi-arid ecosystems where phenological signals are sparse and irregular. This study investigates temporal reconstruction of NDVI under quality masking–induced data gaps, with a specific focus on preserving low-frequency phenological structure rather than maximizing pointwise accuracy. We propose a fully unsupervised reconstruction strategy based on one-dimensional flat morphological closing applied along the temporal dimension, and systematically compare it against common baseline methods, including moving average smoothing, Savitzky-Golay filtering, and harmonic analysis of time series (HANTS). Reconstruction fidelity is first evaluated under controlled cloud simulations using spectral-domain metrics derived from dominant annual and intra-annual harmonics. At a noise level of 0.3, morphological reconstruction achieves a spectral fidelity of 0.93 and an RMSE of 0.02, compared to spectral fidelity value of 0.81 and RMSE of 0.073 for the strongest competing method. The practical implications of reconstruction fidelity are then assessed through unsupervised clustering of real Sentinel-2 NDVI time series. Clustering performance is evaluated using F1-score and precision, both with and without spectral feature augmentation derived from low-order Fourier amplitudes. Morphological reconstruction achieves a mean F1-score of 0.68 compared to 0.59–0.62 for baseline methods and shows minimal improvement (<0.02) after spectral augmentation, indicating that dominant phenological information is already preserved. In contrast, competing methods gain 0.05–0.08 in F1-score after augmentation, suggesting compensation for spectral distortion. Together, these results demonstrate that morphological temporal reconstruction provides a simple, parameter-light, and phenologically consistent alternative for quality-based masking mitigation in NDVI time series, with measurable advantages for downstream unsupervised analysis

1. Introduction

Rangeland ecosystems are among the most widespread land categories worldwide, extending over diverse landscapes and climatic regions. These landscapes are particularly vital in arid and semi-arid regions [1], where they support rural and pastoral communities through maintaining ecological processes and contributing to their livelihoods and economies [2–5]. The rangelands sustain human and ecological well-being by means of the provision of forage, water resources, and a wide range of ecosystem services [6,7]. In Africa alone, hundreds of millions of people depend directly on rangelands for their livelihoods, with livestock production representing the primary land use activity [6–8]. Beyond local subsistence, rangelands also contribute significantly to biodiversity conservation and the maintenance of ecological balance [6,9].

Rangelands are characterized by high spatial and temporal variability, making precise monitoring essential for ecosystem function and pastoral livelihoods. While conventional field surveys are impractical at large scales [10], satellite remote sensing offers an efficient alternative [11,12]. The study of remote sensing imagery provides vital applications across diverse sectors, including environmental management [13]. When enhanced by artificial intelligence [14,15], these technologies

* Corresponding author at: University of Kassel, Kassel, Germany.
E-mail address: agrartechnik@uni-kassel.de (O. Hensel).

https://doi.org/10.1016/j.rineng.2026.110037
Received 23 January 2026; Received in revised form 24 February 2026; Accepted 11 March 2026
Available online 12 March 2026

enable the detailed, timely analysis of vegetation categories across space and time required for sustainable management.

In this context, supervised classification is one of the most effective methods for vegetation monitoring [16–18], heavily relying on high-quality annotated training data [19–21], which serves as the foundation for machine learning algorithms to learn and distinguish between vegetation types. However, collecting unbiased reliable training data is particularly challenging in rangelands [22], where it is also not often feasible to find large, homogeneous areas of a single vegetation type that are larger than the pixel size of any freely available satellite imagery when surveying the field on foot. In this context, unmanned aerial vehicles (UAVs) offer a valuable alternative due to their high-resolution imagery and comprehensive bird's-eye view, allowing researchers to efficiently capture diverse vegetation types across the landscape [22]. Nevertheless, UAV-based surveys face several limitations, including regulatory restrictions, logistical difficulties in remote or insecure areas, and their inability to cover the extensive spatial scales typical of African rangelands. These constraints reduce their practicality for large-area monitoring, despite their usefulness for local validation. As a result, unsupervised learning becomes particularly advantageous and more adaptable, since they do not depend on large training datasets but instead group pixels based on their spectral and temporal properties [23,21,24]. Clustering algorithms are widely recognized as one of the most applied unsupervised approaches [21]. Only a limited number of samples are required for evaluation, making clustering more suitable for vast and data-scarce rangeland environments.

Among freely available multispectral satellites with global coverage, Sentinel-2 provides the highest spatial resolution [14] and frequent revisit times, making it particularly suitable for monitoring vegetation dynamics across extensive rangeland areas. From these data, the Normalized Difference Vegetation Index (NDVI) — derived from the difference between near-infrared (NIR) and red (R) reflectance [25] — has been widely used for vegetation monitoring and classification [26,27,24]. When analyzed as a time series, NDVI captures temporal dynamics of vegetation cover, enabling the detection of patterns and the grouping of areas with similar ecological characteristics [28–30,21,24].

A persistent challenge for time-series-based analysis of optical satellite data is cloud contamination. Seasonal cloud cover frequently obscures surface reflectance, producing artificially low NDVI values and introducing discontinuities into temporal profiles. For instance, Fig. 1 illustrates two consecutive Sentinel-2 NDVI acquisitions from 16 June 2024 and 21 June 2024, where the presence of clouds in Fig. 1b and 1d creates drastic differences despite the short five-day interval. Such distortions corrupt phenological trajectories and degrade the distance relationships on which clustering algorithms rely, particularly in landscapes characterized by fine-scale ecological heterogeneity. As a result, even fully unsupervised methods remain highly sensitive to preprocessing quality, and inadequate temporal restoration can lead to unstable or misleading clustering outcomes.

Addressing these challenges requires more than generic smoothing or gap-filling. For unsupervised clustering to be meaningful, the temporal preprocessing must selectively suppress cloud-induced distortions while preserving phenological structure that differentiates vegetation types. This study adopts a fully unsupervised analysis framework in which temporal restoration is explicitly evaluated through its impact on phenological fidelity and clustering stability.

Within this framework, temporal morphological filtering is employed as an efficient envelope-preserving operation that selectively attenuates impulsive negative artifacts associated with cloud-related data gaps and radiometric artifacts. Unlike linear smoothers that

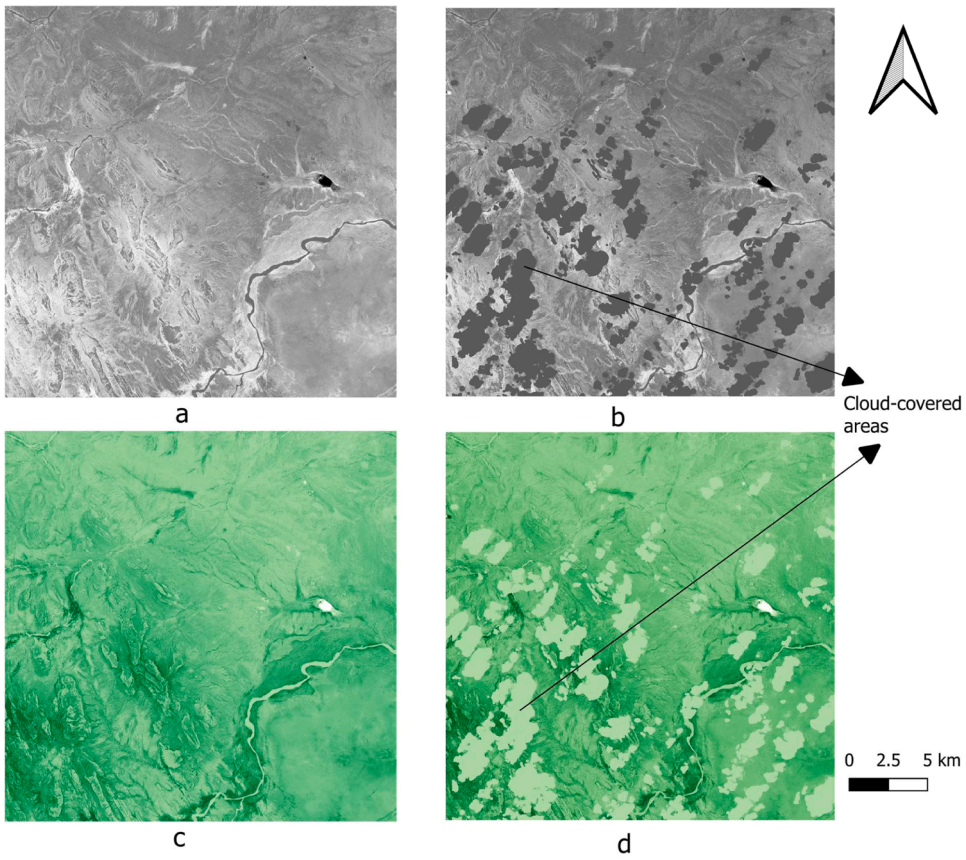

Fig. 1. Sentinel-2 NDVI imagery from two consecutive acquisitions (5-day interval) over the study area in Kenya, illustrating the impact of cloud cover. (a) and (c) show a cloud-free acquisition in grayscale and green-gradient visualization, respectively. (b) and (d) show the subsequent, cloud-contaminated acquisition in grayscale and green-gradient visualization, respectively.

minimize local deviation, morphological filtering operates on the temporal envelope of the signal, enabling preservation of phenological bounds across a range of noise conditions and temporal scales. Restoration robustness is assessed using a spectrum-based phenological fidelity measure that quantifies preservation of dominant seasonal harmonics in both amplitude and phase, providing a principled means of comparing reconstruction methods without reliance on pointwise ground truth. The influence of temporal restoration on unsupervised clustering coherence is further quantified. Additionally, controlled spectral feature augmentation is used to examine redundancy and alignment between reconstructed temporal features and dominant seasonal components. Together, these analyses demonstrate that phenology-aware temporal restoration—evaluated through both simulated cloud degradation and spectral fidelity—plays a critical role in enabling stable, unsupervised vegetation pattern discovery in cloud-affected rangeland environments.

Section 2 reviews related work, followed by Section 3, which integrates the materials and methods, encompassing the study area, data sources, and the proposed analytical framework. Section 4 discusses the results and analysis, while Section 5 is devoted to the conclusion.

2. Cloud mitigation methods for NDVI time series

Cloud mitigation and reconstruction methods for NDVI time series can be broadly categorized according to the dimensionality of information they exploit: spatial, spatio-temporal, and purely temporal approaches [31]. Spatial methods estimate corrupted observations from neighboring pixels under assumptions of land-cover continuity, while spatio-temporal approaches jointly leverage spatial and temporal correlations to constrain reconstruction. In contrast, temporal methods operate exclusively along the time axis, treating each pixel independently.

Although spatial and spatio-temporal techniques can be effective in homogeneous regions, their reliance on spatial similarity limits their applicability in heterogeneous landscapes. For moderate- to coarse-resolution imagery, such as Sentinel-2 composites, spatial reconstruction can blur boundaries between distinct land-cover types and introduce biases that propagate into final applications. This limitation is particularly problematic for unsupervised clustering, where preserving pixel-level temporal identity is essential. Consequently, purely temporal approaches provide a more conservative and interpretable alternative and are the focus of this study.

Within temporal approaches, a fundamental distinction exists between explicit gap-filling methods and implicit filtering-based mitigation strategies. Explicit gap-filling assumes that corrupted observations are known a priori and reconstructs missing values using neighboring valid samples. Representative methods include linear interpolation [32], iterative interpolation schemes [33,34], and learning-based reconstruction models [35,36]. While effective when reliable cloud masks are available, these methods critically depend on accurate identification of corrupted observations

In practice, particularly in dryland and sparsely vegetated environments, low NDVI values may correspond either to cloud contamination or to genuine surface conditions such as bare soil or water bodies. This ambiguity renders gap locations uncertain and often poorly delineated, making explicit gap-filling strategies unreliable.

Mask-free temporal filtering constitutes a widely adopted alternative for NDVI denoising and reconstruction. These methods can be grouped into three categories: (i) local window-based smoothers, (ii) global model-based estimators, and (iii) adaptive or multi-scale filtering schemes. Local smoothers include moving-average and median filters [37], as well as the Savitzky-Golay (SG) filter [38], which performs local polynomial least-squares fitting within a sliding window. Due to its efficiency and simplicity, SG filtering remains a baseline method. It preserves the overall temporal trend while reducing noise and temporary fluctuations in vegetation indices.

Global model-based approaches fit parametric or basis-function representations to the entire time series. For instance, Zhou et al. [39] utilized Harmonic Analysis of Time Series (HANTS) to model NDVI as a sum of sinusoids with iterative outlier rejection. In a similar way, penalized least-squares smoothers like the Whittaker filter [40] recover seasonal structures through explicit smoothness regularization. While these methods effectively suppress noise, their reliance on smooth periodicity may oversimplify phenological transitions that are asymmetric or evolve rapidly.

Adaptive and multi-scale strategies aim to bridge local and global modeling by explicitly accounting for temporal dynamics across scales. State-space formulations, including Kalman and Ensemble Kalman filters, treat vegetation indices as latent dynamical processes and integrate observations sequentially through an evolution model [41]. Decomposition-based frameworks—such as wavelet denoising [42], Singular Spectrum Analysis (SSA) [43], and Seasonal-Trend Decomposition using LOESS (STL) [44,45]—isolate noise components while preserving dominant phenological trends. Despite their flexibility, comparative studies indicate that no single temporal filter consistently outperforms others across varying environmental conditions [46], highlighting the need for methods that balance robustness to cloud contamination with preservation of phenological shape.

Beyond smoothing- and model-based approaches, mathematical morphology [47] has been explored as a shape-preserving alternative for temporal signal reconstruction. Morphological operators, originally developed for image analysis, have been applied to time series to suppress impulsive artifacts while preserving extrema and structural envelopes. In the context of NDVI reconstruction, morphological closing has been used to mitigate cloud-induced negative excursions by selectively filling downward gaps without enforcing global smoothness.

Recent studies [48] have demonstrated the potential of morphological filtering for cloud mitigation in vegetation index time series; however, existing applications primarily focus on pointwise reconstruction accuracy or visual gap filling, with limited evaluation of phenological structure preservation or downstream analytical impact. In contrast, the present study explicitly evaluates morphological reconstruction through spectral-domain phenological fidelity and unsupervised clustering stability, thereby positioning morphological filtering not merely as a denoising tool, but as a phenology-aware preprocessing strategy for unsupervised vegetation analysis.

3. Materials and methods

This section details the physical and technical components of the study, beginning with the description of the rangeland study area and data sources, followed by the formal development of the proposed analytical framework. Unsupervised clustering of vegetation time series is inherently sensitive to distortions in temporal shape, amplitude, and phase. In cloud-prone semi-arid environments, false NDVI drops introduce artificial discontinuities that corrupt temporal similarity relationships, undermining the ability of clustering algorithms to recover meaningful vegetation patterns. To address this limitation, we propose a fully unsupervised pipeline that combines phenology-preserving temporal reconstruction with distance-based clustering. Central to this framework is a morphological filtering strategy that selectively suppresses masking-induced negative artifacts associated with cloud contamination while retaining biologically meaningful phenological structure, thereby stabilizing the temporal geometry required for reliable clustering.

3.1. Study area

The study area is a 25 by 25 km region in Marsabit County, Kenya, extending slightly into Samburu County. (Fig. 2). This area encompasses Ngurunit sub-location and is in the country's northern arid region. This area experiences two rainy seasons, with a short dry phase in January

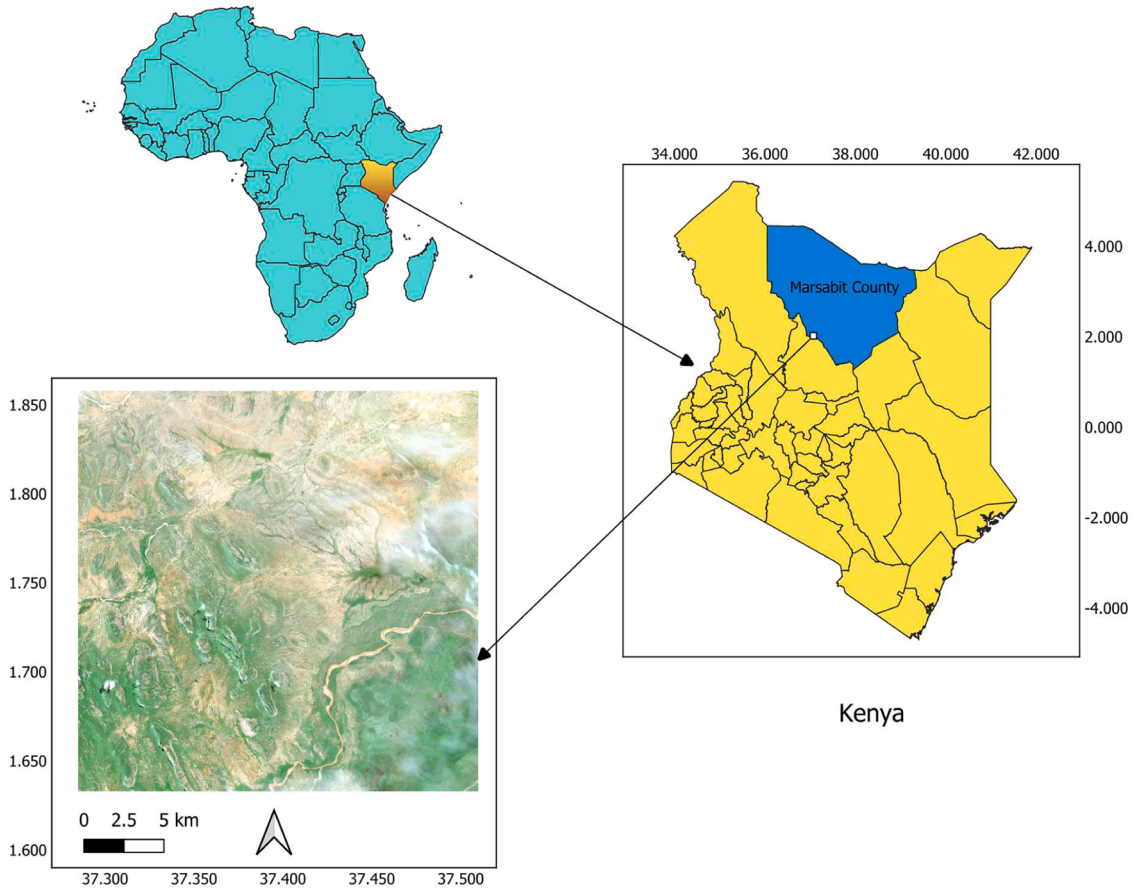

Fig. 2. The location of study area: regional context within Africa and Kenya, and the specific study site in Marsabit County.

and February, followed by a longer rainy period from March to May. A prolonged dry season occurs from July to September, and a shorter rainy season follows from October to December [49]. The annual rainfall varies between 200 mm and 1000 mm, with an average of 254 mm [50]. In Marsabit, pastoralism is the predominant livelihood, with 97 % of the population identifying as either pastoralists or agro-pastoralists [49]. Vegetation mapping in this region is essential for supporting sustainable pastoralism, as it provides crucial insights into the availability and distribution of forage resources. This information is vital for managing grazing patterns and ensuring the long-term viability of pastoralist livelihoods.

3.2. Data sources

For this study, a time series of Sentinel-2-derived NDVI images covering the one-year period from 24 November 2023 to 23 November 2024 was used to capture vegetation dynamics across the study area. The time interval between the images was 5 days. These data provided continuous spectral information over one year, which was then applied in clustering analyses to characterize rangeland vegetation.

Sentinel-2 Level-2A products from the Copernicus Sentinel-2 mission were used in this study. Prior to temporal reconstruction, NDVI time series were computed at 10 m spatial resolution from the red (B04) and near-infrared (B08) bands. To ensure physically meaningful observations, cloud and cloud-shadow pixels were masked using the Sentinel-2 Scene Classification Layer by excluding pixels labeled as cloud shadow, medium- or high-probability cloud, thin cirrus, and snow/ice (classes 3, 8, 9, 10, and 11). NDVI was calculated only for the remaining valid pixels, producing a cloud-filtered time series. This preprocessing step is essential because unmasked cloud-contaminated pixels can introduce spurious negative excursions that do not reflect vegetation phenology, which would distort both temporal reconstruction and downstream unsupervised clustering. Similar SCL-based cloud masking has been widely adopted in remote sensing studies to generate filtered NDVI time series for phenological analysis (e.g., [51]), establishing this approach as a standard and reproducible method. The resulting series forms the basis for both controlled cloud-gap simulations and real-data reconstruction, ensuring that subsequent analyses focus on true vegetation dynamics rather than radiometric artifacts. Masked observations were treated as missing values during temporal reconstruction to avoid introducing artificial low NDVI signals.

Ground-truth data were compiled through a combination of field-based polygon delineation and subsequent refinement using remote sensing sources. Initial polygons were collected directly in the rangelands with the QField mobile application, which enabled GPS-based mapping on smartphones and seamless synchronization with QGIS for data management [52,53]. These polygons were further refined and expanded using UAV imagery, from which ten high-resolution RGB images were captured over representative sites (Fig. 3). In addition to UAV images, commercially acquired Pleiades high-resolution satellite imagery and freely available basemaps (Google Satellite imagery accessed via XYZ tiles in QGIS) were used as supplementary reference material to support visual interpretation and adjustment of polygons. The final ground-truth dataset comprised 107 multi-pixel samples; the distribution across each class is specified in Table 1, representing the total spatial extent used for cluster validation.

Sampling focused on dominant vegetation species within the region, ensuring that local ecological characteristics were adequately represented. Species-level observations were consolidated into broader vegetation types for clustering, a grouping process based on the species' phenological characteristics and local expert knowledge. Ultimately, all samples were assigned to four major land cover classes, namely

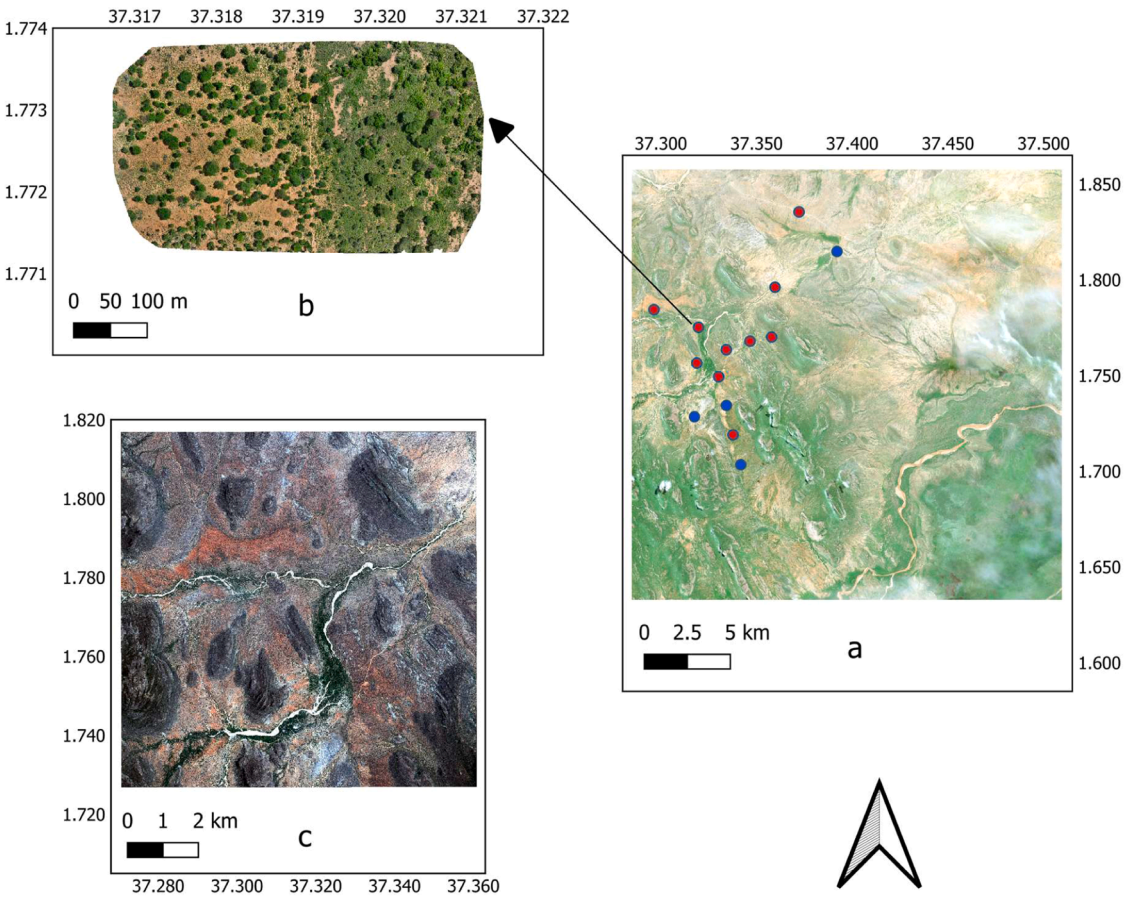

Fig. 3. (a) Ground-truth sample areas: red points represent areas mapped with UAV and/or QField surveys, blue points represent areas derived from Pleiades imagery and/or QField surveys. Each point includes multiple samples. (b) Example UAV image used for ground-truth mapping. (c) Pleiades high-resolution satellite image covering a 10 by 10 km subset of the 25 by 25 km study area.

Table 1
Distribution of vegetation classes and sample sizes.

Classes	Number of samples	Species
Evergreen vegetation	23	Prosopis Prosopis juriflora Boscia spp. (Qalqalcha)
Seasonal woody vegetation	28	Acacia Acacia reficiens Acacia tortilis Bissar Hagar Lachamin
Herbaceous vegetation	27	Shrub-grass mosaic Yabbah Grass
Exposed surface	29	Bare soil Rocky outcrop

evergreen vegetation, seasonal woody vegetation, herbaceous vegetation, and exposed surfaces. To provide clarity on the composition of the reference dataset, the final field-based samples were summarized into four aggregated vegetation classes. It is important to note that species are referred to by their scientific names, except for 'Hagar' and 'Lachamin', for which scientific names could not be found and thus local names were used [2,54]. Table 1 presents the number of samples assigned to each class together with examples of the dominant species represented. This summary helps illustrate how species-level observations were consolidated into broader functional groups for use in the subsequent temporal filtering and clustering analyses. Fig. 4 illustrates the flow diagram, detailing the connection between data sources, the analysis phase, and the performance assessment part.

3.3. Morphological temporal reconstruction

Morphological operators are widely used in image processing to suppress impulsive noise while preserving structural extrema and object boundaries [55,47]. Unlike linear smoothers, which modify signals through local averaging, morphological operations rely on order-statistic transformations that act directly on the signal envelope. This non-linear behavior is particularly well suited to NDVI time series, where cloud contamination typically appears as abrupt negative drops that should be removed without weakening valid vegetation responses.

In this study, we employ the classic flat morphological closing operation to reconstruct NDVI time series along the temporal dimension. Let $(t, \mathbf{p})$ denote the NDVI value at time index t and spatial pixel location $\mathbf{p}$. For a fixed pixel $\mathbf{p}$, morphological closing, denoted by $\bullet$, is applied to the one-dimensional temporal signal $x(t, \mathbf{p})$ and is defined as the composition of dilation ($\oplus$) followed by erosion ($\ominus$) using a flat structuring element B:

$$x(t,\mathbf{p})\cdot B = (x(t,\mathbf{p}) \oplus B) \ominus B. \tag{1}$$

The fundamental morphological operators are defined as [56]

$$(x \oplus B)(t,\mathbf{p}) = \max_{s\in B}\{x(t-s,\mathbf{p})\}, \tag{2}$$

$$(x \ominus B)(t,\mathbf{p}) = \min_{s\in B}\{x(t+s,\mathbf{p})\}. \tag{3}$$

The structuring element B is chosen as a flat, symmetric one-dimensional window of length L. This design choice is deliberate: flat

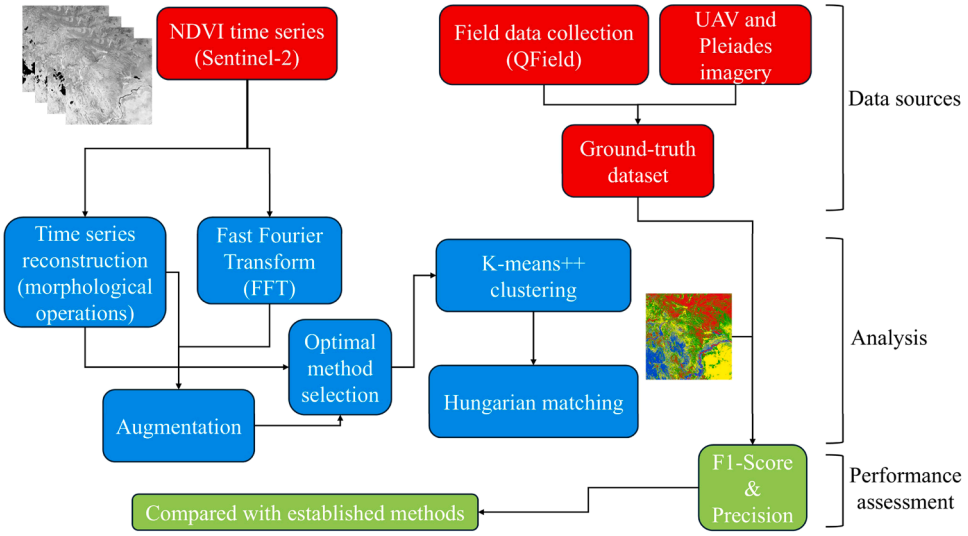

Fig. 4. The flow diagram of the study.

structuring elements impose uniform geometric constraints and avoid introducing additional weighting or shape assumptions, enabling a focused analysis of the intrinsic behavior of morphological closing on phenological signals [47,57].

3.4. Analytical properties and phenological fidelity

The primary objective of morphological closing in this context is to suppress cloud-induced negative artifacts while preserving the intrinsic temporal structure of vegetation dynamics. During dilation, local maxima propagate across narrow temporal depressions, effectively bridging masking-induced temporal gaps. The subsequent erosion restricts this expansion, restoring the signal to its original support without redistributing signal amplitude across neighboring samples. As a result, morphological closing removes noise-related dips while maintaining the amplitude and timing of valid phenological extrema.

To quantify the preservation of biologically meaningful temporal structure, we evaluate phenological fidelity through harmonic analysis of the reconstructed NDVI series. Specifically, we examine the preservation of the first and second harmonic components, which capture the dominant seasonal cycle and sub-seasonal modulation of vegetation dynamics. High harmonic fidelity indicates that the reconstruction preserves both phase and amplitude of underlying phenological oscillations, rather than merely producing a smooth approximation of the signal.

It is important to emphasize that low reconstruction error alone is not sufficient to guarantee phenological integrity. Linear smoothers, including Savitzky-Golay and harmonic-based filters, often reduce Root Mean Square Error (RMSE) by weakening extrema through averaging, which can bias peak magnitudes and compress inter-class variability. In contrast, morphological closing achieves error reduction by selectively removing impulsive noise-induced deviations while preserving the overall phenological shape and sharp temporal transitions. Consequently, morphology can simultaneously attain low RMSE and high spectral fidelity, reflecting a fundamentally different reconstruction mechanism.

These properties are critical for downstream unsupervised analysis, as clustering algorithms are highly sensitive to distortions in temporal distance relationships. By preserving extrema, phase alignment, and temporal asymmetry, morphological reconstruction stabilizes similarity measures in the reconstructed time series, providing a reliable foundation for unsupervised grouping.

3.5. Unsupervised clustering strategy

Following temporal reconstruction, pixels are grouped using the K-means++ clustering algorithm [58]. K-means++ extends standard K-means through probabilistic centroid initialization, improving convergence stability while retaining low computational complexity. Its reliance on simple Euclidean distances makes it particularly sensitive to distortions in temporal shape, amplitude, and phase, and therefore well suited as a conservative baseline for evaluating the quality of temporal reconstruction. While more complex probabilistic or distance-flexible models offer increased robustness, their inherent ability to tolerate local signal irregularities can inadvertently mask residual artifacts in the reconstructed time series.

More expressive clustering models, such as hierarchical methods or Gaussian mixture models, can capture complex cluster geometries but introduce additional modeling assumptions and increased robustness to local temporal distortions. While advantageous in some contexts, such flexibility can obscure the direct impact of temporal preprocessing on phenological similarity. In contrast, the use of K-means++ intentionally imposes minimal structural bias, ensuring that clustering performance is driven primarily by the fidelity of the reconstructed NDVI time series rather than by the clustering model itself. By utilizing a baseline model that provides no built-in compensation for signal noise, we ensure that the reported gains are a direct consequence of improved phenological preservation. Under this formulation, improvements in clustering performance directly reflect improved preservation of phenological structure.

To further assess the completeness of the reconstructed temporal information, we optionally augment the NDVI series with low-dimensional spectral features derived from low-order harmonic components. This augmentation is used diagnostically rather than as a required step: substantial performance gains indicate that critical phenological information is missing from the reconstructed signal, whereas marginal or negligible gains suggest that dominant seasonal structure is already preserved. As demonstrated in the results, spectral augmentation provides limited benefit following morphological reconstruction, indicating that the reconstructed time series alone retains sufficient phenological information for effective unsupervised clustering.

3.6. Cluster-class alignment and evaluation

Because unsupervised clustering produces arbitrary label

assignments, a principled alignment mechanism is required for objective evaluation against reference classes. We employ the Hungarian algorithm [59] to determine the optimal one-to-one correspondence between predicted clusters and reference classes.

Let $C = \{C_1, \ldots, C_K\}$ denote the set of predicted clusters and $G = \{g_1, \ldots, g_K\}$ the reference classes. For each pair (c_i, g_j), we compute the F1-score [60]:

$$\mathrm{F1}\left(c_i, g_j\right) = \frac{2P\left(c_i, g_j\right) R\left(c_i, g_j\right)}{P\left(c_i, g_j\right) + R\left(c_i, g_j\right)}, \tag{4}$$

where precision P and recall R are defined as

$$P\left(c_i, g_j\right) = \frac{\left|c_i \cap g_j\right|}{\left|c_i\right|}, \tag{5}$$

$$R\left(c_i, g_j\right) = \frac{\left|c_i \cap g_j\right|}{\left|g_j\right|}. \tag{6}$$

The F1-score balances over-assignment and omission errors, making it particularly suitable for evaluating cluster-class correspondence in vegetation mapping, as a high F1-score requires a balance of both precision and recall in imbalanced scenarios [61]. The assignment cost is defined as

$$\mathrm{Cost}\left(c_i, g_j\right) = 1 - \mathrm{F1}\left(c_i, g_j\right), \tag{7}$$

and the Hungarian algorithm finds the permutation σ that minimizes the total cost:

$$\min_{\sigma \in S_K} \sum_{i=1}^{K} C_{i,\sigma(i)}, \tag{8}$$

where S_K denotes the set of all permutations of $\{1, \ldots, K\}$. This alignment enables consistent relabeling of clusters and objective quantitative comparison across reconstruction and filtering strategies.

4. Results, analysis and discussion

This section quantitatively evaluates the proposed framework through controlled reconstruction experiments and subsequent unsupervised clustering analysis. First, we analyze the behavior of morphological closing and baseline temporal reconstruction methods under synthetic cloud-like perturbations, assessing both pointwise reconstruction accuracy and preservation of spectral structure. Second, we evaluate clustering performance on real Sentinel-2 NDVI time series processed by each method, reporting F1-score and precision with and without spectral feature augmentation. Given the sparse and aggregated nature of available reference polygons, these metrics are interpreted comparatively rather than as absolute measures of classification accuracy, providing a consistent external benchmark for assessing how temporal reconstruction influences phenological fidelity and cluster separability in an unsupervised setting.

For comparison, we select moving average smoothing (refer to [37]), Savitzky-Golay filtering [38], and HANTS [39] as representative baselines spanning three commonly used classes of temporal reconstruction methods: local smoothing, local polynomial approximation, and global harmonic fitting. These methods are widely adopted in vegetation time series analysis and represent fundamentally different assumptions about noise, gaps, and seasonal structure. Their inclusion enables a principled comparison between morphology-based reconstruction and established approaches that prioritize smoothness or spectral compactness, allowing us to attribute observed differences in clustering behavior to the underlying reconstruction paradigm rather than to implementation-specific details.

4.1. Temporal reconstruction under simulated cloud contamination

We first evaluate temporal reconstruction performance under controlled cloud-like perturbations using simulated NDVI gaps. This experiment shows the behavior of different reconstruction mechanisms under known corruption levels before assessing their impact on downstream clustering.

Reference signal construction: Noise-reduced reference NDVI time series $\hat{x}(t, \mathbf{p})$ are obtained by fitting low-order harmonic models (HANTS) independently to each pixel. Two harmonics are retained to represent the dominant annual cycle and low-order intra-annual variability characteristic of dryland vegetation, while higher-order components are excluded to avoid fitting short-term fluctuations and residual noise. The resulting signal $\hat{x}$ serves as a cloud-free reference and is used exclusively for controlled simulation and evaluation. Importantly, downstream analyses on real NDVI time series ensure that conclusions do not rely on the HANTS reference.

Cloud gap simulation: Cloud contamination is modeled as temporal gaps rather than additive noise, reflecting the physical nature of cloud effects in optical remote sensing. For a prescribed corruption level $\rho \in [0, 1]$, a fraction ρ of pixel-time samples is masked and assigned a zero value, producing strong negative excursions typical of cloud-contaminated NDVI observations. While this zero-masking constitutes a conservative, worst-case perturbation for per-pixel temporal reconstruction, subsequent evaluation on real NDVI time series verifies the method's robustness under realistic satellite noise and cloud conditions.

Masking is performed in a frame-dependent manner: each temporal frame is assigned a different cloud coverage level, resulting in heterogeneous corruption across time. While the overall fraction of masked samples equals ρ, individual frames may be nearly cloud-free or heavily obscured. This procedure reproduces key characteristics of real NDVI datasets, including temporally clustered gaps and inter-frame variability, without introducing artificial signal values.

The corrupted NDVI sequence is defined as

$$x_\rho(t, \mathbf{p}) = \hat{x}(t, \mathbf{p}) \cdot m(t, \mathbf{p}), \tag{9}$$

where $m(t, \mathbf{p}) \in \{0, 1\}$ denotes a binary cloud mask, with values indicating valid or cloud-contaminated observations.

Fig. 5 illustrates an example of the noise-reduced reference signal $\hat{x}(t, \mathbf{p})$ and its corresponding corrupted realization $x_{0.2}(t, \mathbf{p})$ for a single pixel.

Reconstruction methods: Each corrupted time series x_ρ is processed using moving-average smoothing, SG filtering, HANTS re-fitting, and the proposed morphological closing. Linear smoothing and SG filtering employ a fixed temporal window of five samples, corresponding to approximately one month of Sentinel-2 observations. HANTS is re-applied with the same harmonic order as the reference signal.

Unless stated otherwise, morphological reconstruction is performed using a classic flat symmetric closing operation with structuring element length $L = 5$, selected to reflect typical short-duration cloud gaps in the dataset. This configuration selectively suppresses negative deviations while limiting peak expansion, preserving both amplitude and temporal structure.

Evaluation metrics: Reconstruction fidelity is assessed in the spectral domain by comparing the dominant harmonic components of the reconstructed signal, $x_\rho^{rec}(t, \mathbf{p})$, to the reference, $\hat{x}(t, \mathbf{p})$. Each signal is decomposed into its first and second harmonics:

$$\hat{x}(t) \approx a_0 + \sum_{k=1}^{2} a_k \cos\left(\frac{2\pi k t}{T}\right) + b_k \sin\left(\frac{2\pi k t}{T}\right), \tag{10}$$

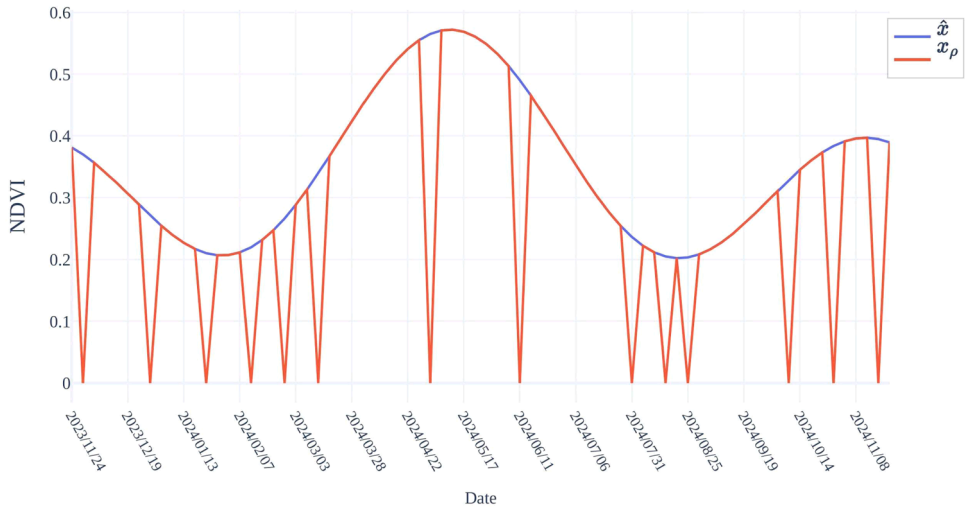

Fig. 5. Example NDVI time series for a single pixel, showing the noise-reduced reference signal $\hat{x}(t, \mathbf{p})$ and its cloud-corrupted counterpart $x_\rho(t, \mathbf{p})$, generated using a noise level of $\rho = 0.2$.

$$x_\rho^{\text{rec}}(t) \approx \widetilde{a}_0 + \sum_{k=1}^{2} \widetilde{a}_k \cos\left(\frac{2\pi k t}{T}\right) + \widetilde{b}_k \sin\left(\frac{2\pi k t}{T}\right), \tag{11}$$

where T is the length of one year in frames. The amplitude of each harmonic is $A_k = \sqrt{a_k^2 + b_k^2}$ and $\widetilde{A}_k = \sqrt{\widetilde{a}_k^2 + \widetilde{b}_k^2}$, while the phase is $\phi_k = \arctan 2(b_k, a_k)$ and $\widetilde{\phi}_k = \arctan 2(\widetilde{b}_k, \widetilde{a}_k)$.

Amplitude and phase fidelity for each harmonic are defined as

$$F_k^{\text{amp}} = 1 - \frac{|\widetilde{A_k} - A_k|}{A_k}, \tag{12}$$

$$F_k^{\text{phase}} = 1 - \frac{|\widetilde{\phi_k} - \phi_k|}{\pi}. \tag{13}$$

A combined spectral fidelity metric can then be computed as [44]

$$F^{\text{spectral}} = \frac{1}{2} \sum_{k=1}^{2} \frac{F_k^{\text{amp}} + F_k^{\text{phase}}}{2}. \tag{14}$$

Reconstruction fidelity is assessed in the spectral domain by comparing the dominant harmonic components of the reconstructed NDVI signal, $x_\rho^{\text{rec}}(t,\mathbf{p})$, to the reference signal, $\hat{x}(t,\mathbf{p})$, on a per-pixel basis. For each spatial location $\mathbf{p}$, both signals are decomposed into their first and second harmonic components as

$$\hat{x}(t, \mathbf{p}) \approx a_0(\mathbf{p}) + \sum_{k=1}^{2} \left[a_k(\mathbf{p}) \cos\left(\frac{2\pi k t}{T}\right) + b_k(\mathbf{p}) \sin\left(\frac{2\pi k t}{T}\right) \right], \tag{15}$$

$$x_\rho^{\text{rec}}(t, \mathbf{p}) \approx \widetilde{a}_0(\mathbf{p}) + \sum_{k=1}^{2} \left[\widetilde{a}_k(\mathbf{p}) \cos\left(\frac{2\pi k t}{T}\right) + \widetilde{b}_k(\mathbf{p}) \sin\left(\frac{2\pi k t}{T}\right) \right], \tag{16}$$

where T denotes the number of temporal frames per year.

For each harmonic k and pixel $\mathbf{p}$, the amplitude and phase are defined as

$$A_k(\mathbf{p}) = \sqrt{a_k^2(\mathbf{p}) + b_k^2(\mathbf{p})}, \ \phi_k(\mathbf{p}) = \arctan2(b_k(\mathbf{p}), a_k(\mathbf{p})), \tag{17}$$

$$\widetilde{A_k}(\mathbf{p}) = \sqrt{\widetilde{a_k^2}(\mathbf{p}) + \widetilde{b_k^2}(\mathbf{p})}, \ \widetilde{\phi_k}(\mathbf{p}) = \arctan2(\widetilde{b_k}(\mathbf{p}), \widetilde{a_k}(\mathbf{p})). \tag{18}$$

Pixel-wise amplitude and phase fidelity for harmonic k are then defined as

$$F_k^{\text{amp}}(\mathbf{p}) = 1 - \frac{|\widetilde{A_k}(\mathbf{p}) - A_k(\mathbf{p})|}{A_k(\mathbf{p})}, \tag{19}$$

$$F_k^{\text{phase}}(\mathbf{p}) = 1 - \frac{|\widetilde{\phi_k}(\mathbf{p}) - \phi_k(\mathbf{p})|}{\pi}. \tag{20}$$

The spectral fidelity for pixel $\mathbf{p}$ is computed by averaging amplitude and phase fidelity across harmonics [44]:

$$F^{\text{spectral}}(\mathbf{p}) = \frac{1}{2} \sum_{k=1}^{2} \frac{F_k^{\text{amp}}(\mathbf{p}) + F_k^{\text{phase}}(\mathbf{p})}{2}. \tag{21}$$

Finally, the reported spectral fidelity is obtained by averaging over all spatial pixels:

$$\overline{F}^{\text{spectral}} = \frac{1}{|\mathscr{P}|} \sum_{\mathbf{p} \in \mathscr{P}} F^{\text{spectral}}(\mathbf{p}), \tag{22}$$

where $\mathscr{P}$ denotes the set of all evaluated pixels.

This metric is a task-specific composite diagnostic constructed from standard harmonic amplitude and phase descriptors commonly used in seasonal time-series and phenological analysis [44]. By focusing on the dominant seasonal modes, it directly quantifies preservation of phenological amplitude and timing, which are critical for phenology-driven applications and unsupervised clustering.

Pointwise reconstruction accuracy is additionally quantified using the Root Mean Square Error (RMSE):

$$\text{RMSE} = \sqrt{\frac{1}{|\Omega|} \sum_{(t,\mathbf{p}) \in \Omega} \left(x_\rho^{\text{rec}}(t, \mathbf{p}) - \hat{x}(t, \mathbf{p}) \right)^2}, \tag{23}$$

where $\Omega = \tau \times \mathscr{P}$ denotes the set of all evaluated time-pixel pairs.

While RMSE penalizes all deviations equally, including short-term fluctuations and residual noise, the spectral fidelity metric emphasizes preservation of dominant seasonal structure. Together, these complementary measures ensure that conclusions are not dependent on a single evaluation criterion and allow separation of pointwise accuracy from phenological integrity.

Results: The comparative evaluation under increasing synthetic cloud contamination reveals clear and consistent trends across both spectral fidelity and pointwise error metrics. In terms of spectral fidelity (Fig. 6), morphological closing exhibits the strongest robustness to missing observations at all noise levels. While SG and temporal averaging show nearly identical behavior, both suffer substantial

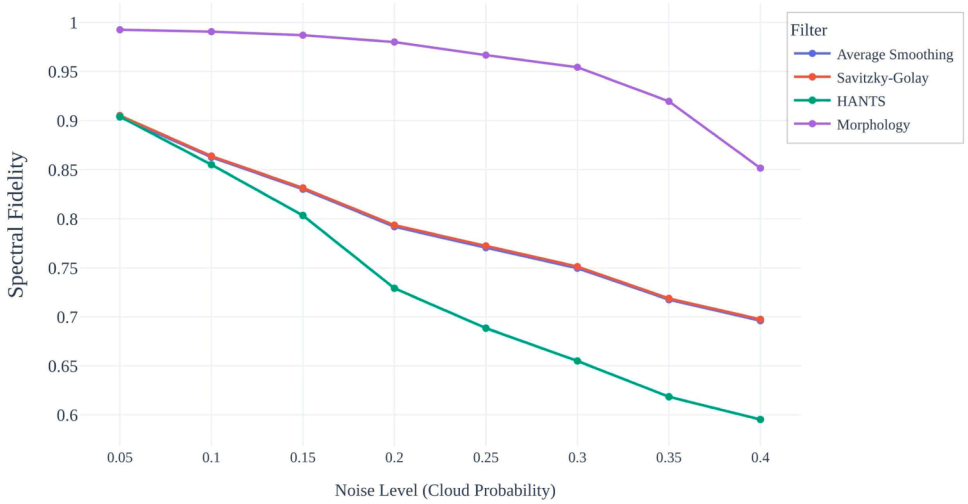

Fig. 6. Impact of noise levels on the spectral fidelity of different reconstruction methods.

degradation as noise increases. HANTS performs worst in this setting, indicating that harmonic refitting under aggressive frame-wise corruption fails to preserve dominant phenological components. At a representative noise level of 0.3, morphological reconstruction retains a spectral fidelity of approximately 0.95, compared to 0.75 for both SG and averaging, and only 0.65 for HANTS. This gap demonstrates that morphology most effectively preserves the amplitude-phase structure of biologically meaningful seasonal harmonics under realistic cloud disturbance.

Pointwise reconstruction accuracy, quantified by RMSE, is shown in Fig. 7. SG filtering consistently yields the highest RMSE, reflecting its tendency to oversmooth and distort cloud-induced gaps rather than explicitly mitigate them. HANTS achieves lower error than averaging only at very low noise levels, where the harmonic model remains well constrained. However, beyond this regime, averaging becomes more stable than HANTS as missing data increases. Morphological closing again outperforms all baselines, achieving the lowest RMSE across all noise levels. At a noise level of 0.3, morphology reduces RMSE to approximately 0.02, compared to 0.07 for averaging, 0.088 for HANTS, and 0.089 for SG.

The divergence between spectral fidelity and RMSE trends for some baselines highlights that low pointwise error alone does not guarantee preservation of phenologically relevant dynamics. From a signal processing perspective, this behavior reflects the fundamentally different assumptions underlying the reconstruction methods. Harmonic and smoothing-based approaches implicitly assume global smoothness or periodicity and tend to redistribute localized distortions across the time series, which can attenuate narrow phenological transitions or shift seasonal timing. In contrast, temporal morphological closing is designed to suppress sparse, impulsive negative deviations while preserving the upper temporal envelope of the signal. This makes it particularly well suited to cloud-contaminated NDVI time series, where corruption primarily appears as abrupt negative drops or gaps.

Under such conditions, morphological reconstruction simultaneously minimizes numerical deviation and preserves dominant seasonal amplitude and phase, a combination not achieved by the evaluated linear or harmonic-based alternatives. At the same time, these results clarify that the advantage of morphology is conditional: in regimes dominated by symmetric noise, prolonged missing observations, or overlapping seasonal modes, envelope-based operations may introduce bias or lose interpretability. This distinction motivates the comparative analysis presented here and underscores the importance of matching reconstruction assumptions to the structure of the underlying signal.

Fig. 8 examines the sensitivity of spectral fidelity to the structuring element length L used in the morphological reconstruction under increasing noise levels. For small windows ($L = 3$), fidelity degrades

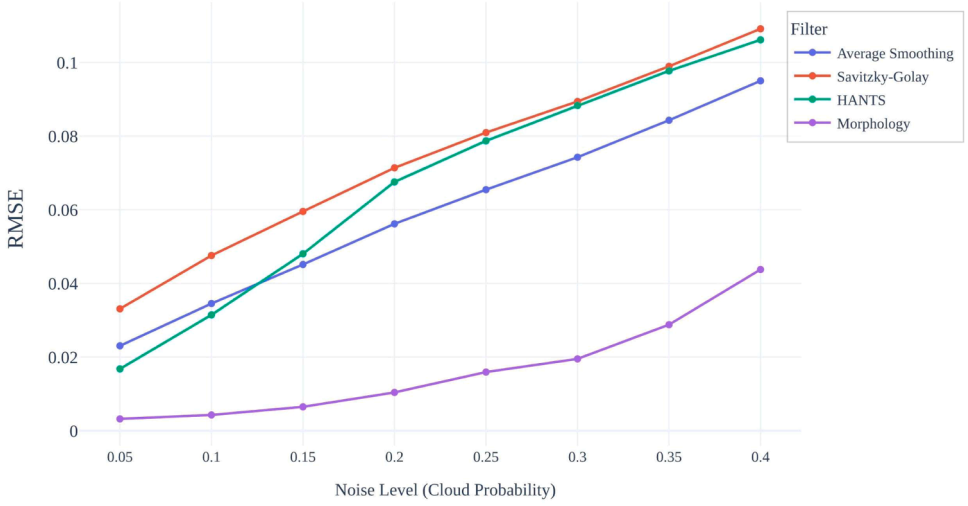

Fig. 7. Impact of noise levels on the RMSE of different reconstruction methods.

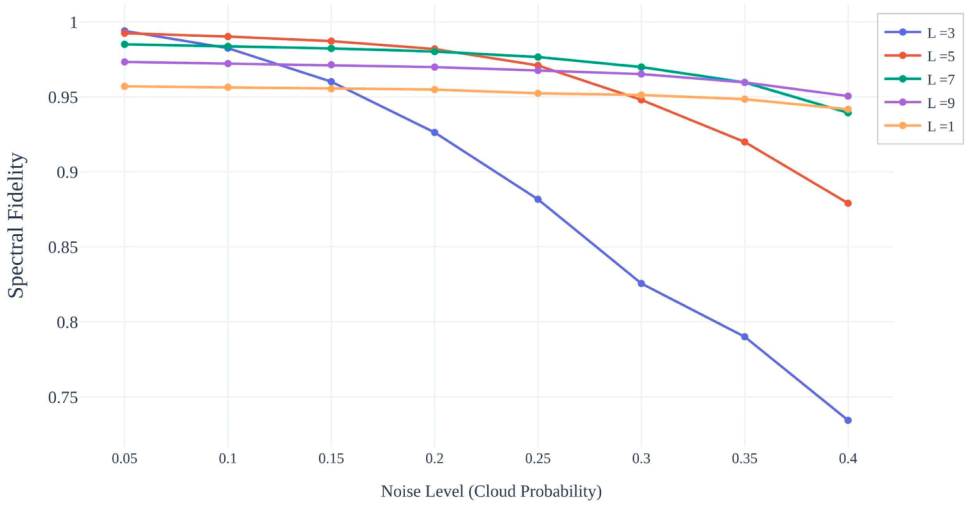

Fig. 8. Combined spectral fidelity as a function of noise level for different structuring element lengths L.

rapidly as noise increases, indicating insufficient gap filling when cloud-induced dips span multiple consecutive frames. In contrast, moderate window sizes ($L = 5$ and $L = 7$) maintain consistently high fidelity across the full range of tested noise levels.

Larger structuring elements ($L \geq 9$) exhibit increased robustness to noise but show a systematic reduction in fidelity even at low corruption levels. This behavior reflects excessive temporal expansion during dilation, which progressively distorts narrow phenological transitions. Within the temporal resolution and phenological regime considered in this study, these results indicate a broad operating range in which reconstruction performance is stable, while also highlighting the trade-off between gap tolerance and phenological distortion.

Overall, the results demonstrate that the proposed morphological reconstruction is not strongly sensitive to moderate variations in L. Window lengths in the range $L = 5$–7 provide a stable operating regime that effectively bridges cloud-induced gaps while preserving seasonal harmonic structure. Unless stated otherwise, a representative value of $L = 7$ is used in subsequent experiments.

Practical implementation considerations: From an operational perspective, temporal morphological reconstruction offers favorable computational and implementation characteristics. The method relies on local max-min operations along the temporal axis, resulting in linear complexity with respect to time series length and negligible memory overhead. Unlike harmonic fitting or learning-based gap-filling approaches, it does not require parameter estimation, iterative optimization, or training data, which simplifies large-scale deployment. In practice, runtime is comparable to simple smoothing filters and substantially lower than harmonic-based methods, making the approach suitable for processing dense Sentinel-2 NDVI archives. The method involves a single intuitive parameter—the temporal structuring element length—which can be selected based on expected phenological duration, facilitating reproducibility and integration into existing remote sensing processing pipelines.

4.2. Unsupervised clustering of real NDVI time series

This subsection evaluates the impact of temporal reconstruction and spectral feature augmentation on unsupervised clustering of real Sentinel-2 NDVI time series. Unlike the controlled simulations in the previous subsection, this analysis reflects practical conditions where ground truth labels are sparse and phenological variability is spatially heterogeneous. We examine how different preprocessing strategies affect cluster separability, stability, and correspondence to reference vegetation classes.

Augmenting NDVI time series with spectral features: Spectral feature augmentation refers to the enrichment of the original NDVI time series with a small set of complementary features derived from its dominant harmonic content. While clustering based solely on temporal NDVI trajectories captures phenological timing and waveform shape, it may insufficiently encode differences in seasonal strength and modulation, particularly in heterogeneous rangeland environments where multiple vegetation classes exhibit similar temporal phases but differ in amplitude.

In this study, spectral features are computed directly from the raw, unfiltered NDVI time series to decouple augmentation from any specific reconstruction method. For each pixel, the first and second harmonic amplitudes, $A_1(\mathbf{p})$ and $A_2(\mathbf{p})$, defined in the previous subsection, are extracted and used as spectral descriptors. The DC component $a_0(\mathbf{p})$ is intentionally excluded, as it reflects only the mean NDVI level and does not convey phenological dynamics. Prior to concatenation with the time-domain signal, each harmonic amplitude is transformed using a log $(1 + A_k(\mathbf{p}))$ mapping. This transformation compresses the dynamic range of spectral magnitudes, mitigates the influence of extreme amplitudes, and stabilizes Euclidean distance computations during clustering, while preserving relative phenological contrasts.

The role of spectral augmentation is therefore not to replace temporal reconstruction, but to compensate for phenological information that may be weakly expressed in the time domain alone. For reconstruction methods that distort or weaken dominant harmonic amplitudes, augmentation can improve cluster separability by explicitly reintroducing low-frequency seasonal structure. Conversely, when temporal reconstruction preserves the harmonic amplitudes A_1 and A_2 with high fidelity, spectral augmentation is expected to provide limited additional benefit, serving primarily as a consistency check on phenological preservation.

Results: Tables 2 and 3 report class-wise and mean clustering performance for real Sentinel-2 NDVI time series reconstructed using different temporal filters, evaluated with and without spectral feature augmentation. Performance differences across methods and classes reflect variations in phenological amplitude, temporal contrast, and spatial separability.

The unfiltered baseline highlights fundamental differences in clustering difficulty across land-cover classes. Exposed surfaces achieve high precision and F1-scores even without temporal reconstruction, owing to their low temporal variability and stable NDVI signatures, which form compact and well-separated clusters. Herbaceous and seasonal woody vegetation exhibit moderate baseline performance, as cloud-induced distortions obscure differences in seasonal amplitude and timing,

Table 2
Class-wise and mean F1-score for unsupervised NDVI time series clustering under different reconstruction filters, with and without spectral feature augmentation.

Filter	Augmentation	Evergreen	Seasonal woody	Herbaceous	Exposed surface	Mean
None	…	0.0000	0.6739	0.7453	0.9693	0.5971
	✓	0.2105	0.6634	0.4554	0.9937	0.5808
Average smoothing	…	0.0000	0.6984	0.7097	0.9753	0.5958
	✓	0.2472	0.6952	0.6610	0.9811	0.6461
Savitzky-Golay	…	0.0000	0.6947	0.7342	0.9753	0.6011
	✓	0.2245	0.6825	0.5370	0.9811	0.6063
HANTS	…	0.1463	0.6235	0.6625	0.9634	0.5989
	✓	0.2410	0.6728	0.6667	0.9937	0.6435
Morphology	…	0.2500	0.6813	0.8743	0.9693	0.6937
	✓	0.2727	0.6957	0.8957	0.9693	0.7084

Table 3
Class-wise and mean precision for unsupervised NDVI time-series clustering under different reconstruction filters, with and without spectral feature augmentation.

Filter	Augmentation	Evergreen	Seasonal woody	Herbaceous	Exposed surface	Mean
None	…	0.0000	0.5794	0.7229	0.9405	0.5607
	✓	0.2000	0.5360	1.0000	0.9875	0.6809
Average smoothing	…	0.0000	0.5893	0.7143	0.9518	0.5638
	✓	0.3143	0.5489	0.9750	0.9750	0.7033
Savitzky-Golay	…	0.0000	0.5841	0.7250	0.9518	0.5652
	✓	0.2500	0.5373	0.9667	0.9750	0.6822
HANTS	…	0.2143	0.5699	0.6463	0.9294	0.5900
	✓	0.3448	0.5214	1.0000	0.9875	0.7134
Morphology	…	0.8000	0.5905	0.8202	0.9405	0.7878
	✓	0.7500	0.5981	0.8588	0.9405	0.7869

limiting separability.

Evergreen vegetation remains the most challenging class, exhibiting zero F1-scores for several reconstruction methods. These zero values indicate complete misclassification (i.e., zero recall), rather than numerical artifacts, and arise from the combination of weak intrinsic seasonality, low temporal contrast, limited sample size, and pronounced spatial mixing at Sentinel-2 resolution. Across this semi-arid landscape, evergreen vegetation is sparse and frequently intermixed with other vegetation types, producing mixed NDVI signals that are inherently difficult to separate using unsupervised temporal features alone, regardless of reconstruction quality.

Without spectral augmentation, clustering performance is dominated by the quality of temporal reconstruction. Morphological reconstruction achieves the highest mean F1-score (0.6937) compared to Savitzky–Golay (0.6011), HANTS (0.5989), moving average (0.5958), and no filtering (0.5971). This advantage is most pronounced for the Herbaceous class, where morphology reaches an F1-score of 0.8743, whereas alternative methods range between 0.6625 (HANTS) and 0.7342 (Savitzky–Golay). For Evergreen vegetation, morphology increases F1 from 0.0000 under smoothing methods to 0.2500, indicating partial recovery of separability under low seasonal contrast conditions. In contrast, moving average and Savitzky–Golay filtering reduce seasonal amplitudes through local averaging, while HANTS introduces residual harmonic distortions that weaken discrimination despite suppressing cloud-induced noise.

Across all classes, morphological reconstruction also yields consistently higher mean precision (0.7878 without augmentation) than competing methods (ranging from 0.5607 to 0.5900). This behavior is particularly evident for Evergreen vegetation, where precision reaches 0.8000 under morphology compared to $\leq$ 0.2143 for other filters, reflecting more stable and conservative cluster assignments despite inherently limited recall.

The impact of spectral feature augmentation is method-dependent. For reconstruction methods that distort dominant low-frequency components, augmentation provides measurable benefits. For example, mean F1-score increases from 0.5958 to 0.6461 for moving average filtering and from 0.5989 to 0.6435 for HANTS. In contrast, morphological reconstruction shows only a modest change (0.6937 to 0.7084), and mean precision remains essentially unchanged (0.7878 to 0.7869), indicating that dominant seasonal structure is largely preserved prior to augmentation.

In contrast, morphological reconstruction exhibits negligible sensitivity to spectral augmentation. Both class-wise and mean performance remain effectively unchanged after augmentation, indicating that the reconstructed time series already retain the dominant harmonic content and phenological shape required for clustering. This invariance provides direct evidence that augmentation does not contribute additional discriminative information beyond what is preserved by morphological reconstruction itself. The absence of augmentation gains therefore reflects completeness of the reconstructed temporal representation rather than saturation or ceiling effects.

Overall, these results confirm that phenological fidelity in temporal reconstruction is the primary determinant of unsupervised clustering performance. Spectral augmentation acts as a compensatory mechanism when reconstruction degrades low-frequency seasonal information, but offers no benefit when dominant temporal structure is preserved. The consistently strong and augmentation-invariant performance of morphological reconstruction therefore provides robust evidence of its effectiveness for unsupervised phenological analysis under cloud-affected conditions.

Qualitative reconstruction analysis: To complement the quantitative metrics, we present a qualitative comparison of reconstructed NDVI time series for representative vegetation classes. These examples were selected from a broader population of randomly sampled pixels to illustrate the characteristic behaviors captured by the aggregate statistical metrics. Fig. 9 presents representative NDVI reconstruction examples for evergreen vegetation, seasonal woody vegetation, herbaceous vegetation, and exposed surfaces, spanning a wide range of phenological regimes and noise sensitivities. This qualitative assessment illustrates how different temporal filters interact with class-specific NDVI dynamics under real cloud contamination.

In accordance with other works [62,63], evergreen vegetation (Fig. 9a) exhibits low seasonal amplitude and is therefore particularly sensitive to cloud-induced negative spikes. While smoothing-based and harmonic methods reduce these distortions, they also weaken subtle seasonal variations and bias the baseline NDVI level. Morphological

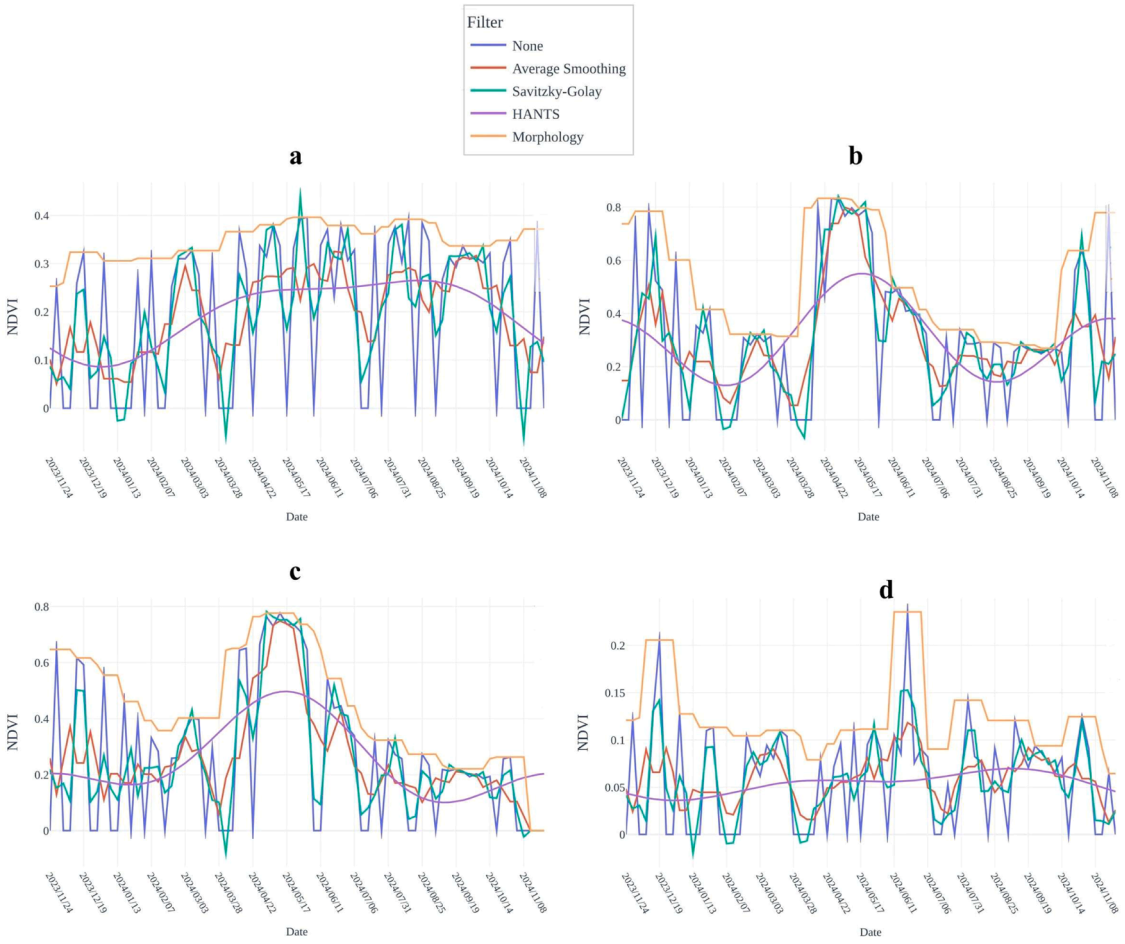

Fig. 9. Example reconstructions of real NDVI time series for four land-cover classes: (a) evergreen vegetation with low seasonal amplitude, (b) seasonal woody vegetation with moderate phenological modulation, (c) herbaceous vegetation exhibiting rapid seasonal transitions, and (d) exposed surfaces dominated by noise.

reconstruction effectively removes transient dips while preserving the signal profile and weak seasonal structure, resulting in a temporally conservative reconstruction that avoids introducing artificial phenology.

Seasonal woody vegetation (Fig. 9b) shows smoother yet more distinct seasonal modulation. Local smoothing and Savitzky-Golay filtering dampen peak amplitudes and broaden transition phases, while harmonic reconstruction enforces globally smooth trajectories that may misalign with localized phenological variability. In contrast, morphological reconstruction retains both the timing and magnitude of seasonal extrema while selectively mitigating anomalies.

Herbaceous vegetation (Fig. 9c) is characterized by rapid green-up, sharp seasonal peaks, and abrupt senescence. These high-frequency transitions are substantially smoothed by conventional filters and partially distorted by harmonic reconstruction. Morphological reconstruction more faithfully preserves peak amplitude and temporal localization, consistent with its superior spectral fidelity and improved clustering performance for this class.

For exposed surfaces (Fig. 9d), NDVI variability is dominated by noise rather than phenology. While all methods reduce extreme deviations, smoothing and harmonic approaches may introduce false seasonal structure. Morphological reconstruction remains conservative, removing transient distortions without imposing artificial temporal patterns.

Overall, the qualitative results confirm that morphological reconstruction consistently mitigates cloud-induced anomalies while preserving phenologically meaningful temporal structure across vegetation types. In contrast, smoothing and harmonic methods reduce noise at the expense of weakened amplitudes, temporal blurring, or structural distortion, reinforcing the quantitative findings. Fig. 10 illustrates the clustered rangeland in Marsabit County, Kenya.

5. Conclusion

This study evaluated temporal reconstruction of cloud-affected NDVI time series with emphasis on preserving phenological structure for unsupervised analysis. One-dimensional morphological closing provided a fully unsupervised and computationally efficient reconstruction strategy that selectively mitigates cloud-induced negative distortions while maintaining seasonal shape and phase alignment.

In unsupervised clustering of Sentinel-2 NDVI time series, morphological reconstruction achieved the highest mean F1-score both without (0.6937) and with (0.7084) spectral augmentation, outperforming Savitzky–Golay (0.6011), HANTS (0.5989), moving average (0.5958), and the unfiltered baseline (0.5971). The improvement is particularly pronounced for Herbaceous vegetation (F1 = 0.8743 without augmentation). Mean precision further confirms this advantage, with morphology reaching 0.7878 without augmentation, substantially exceeding all other methods ($\leq$ 0.5900). Unlike competing approaches, morphological reconstruction shows minimal sensitivity to spectral augmentation, indicating that dominant seasonal information is already preserved in the reconstructed signals.

The method assumes that cloud contamination primarily introduces negative deviations and depends on appropriate selection of the temporal structuring element. Performance may decrease under prolonged data gaps, symmetric noise, or markedly different seasonal regimes, and

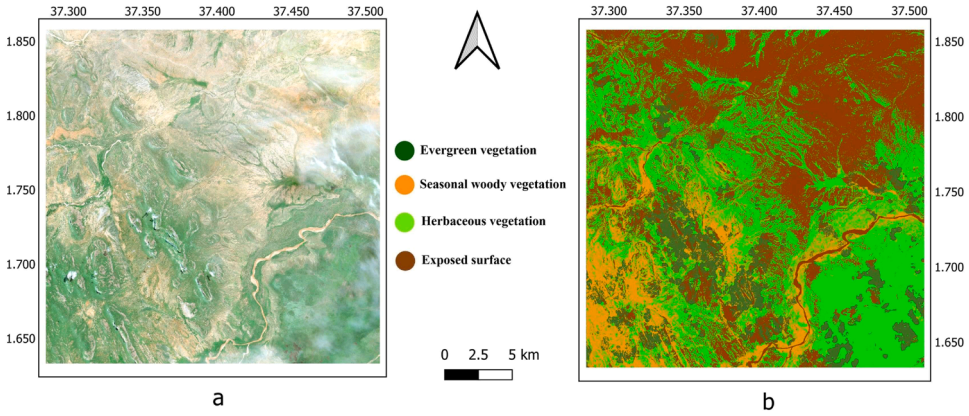

Fig. 10. (a) True color image (b) corresponding final clustered output for the study area.

transferability beyond the evaluated environmental context requires further validation.

Future work may explore adaptive or multi-scale structuring elements, phenology-informed parameter selection, and integration with multi-sensor or learning-based frameworks. Due to its linear computational complexity, absence of training requirements, and simple one-dimensional operations, the proposed approach is well suited for scalable and near–real-time NDVI preprocessing pipelines.

Overall, the results demonstrate that preserving temporal structure—rather than applying generic smoothing—is critical for reliable unsupervised phenological analysis, and morphological reconstruction provides a robust and operationally practical solution.

Declaration of AI use

During the preparation of this manuscript, generative AI tools were used solely to assist with language refinement, structuring, and organizational clarity. The authors critically reviewed, verified, and approved all content and accept full responsibility for the integrity and accuracy of the final manuscript.

CRediT authorship contribution statement

Hooman Hosseini: Writing – review & editing, Writing – original draft, Visualization, Validation, Software, Methodology, Investigation, Formal analysis, Data curation, Conceptualization. **Brigitte Kaufmann:** Writing – review & editing, Supervision, Conceptualization. **Oliver Hensel:** Writing – review & editing, Supervision, Resources, Funding acquisition. **Abozar Nasirahmadi:** Writing – review & editing, Supervision, Project administration, Conceptualization.

Declaration of competing interest

The authors declare that they have no known competing financial interests or personal relationships that could have appeared to influence the work reported in this paper.

Acknowledgements

This study was carried out within the framework of the InfoRange project, supported by the German Federal Ministry of Research, Technology and Space (Bundesministerium für Forschung, Technologie und Raumfahrt, BMFTR) under grant number 01LL2201B. We also acknowledge Sebastian Schmidt and Zakieh Alizadehsani (University of Kassel) for their support in data collection, as well as Raphael M. Gurleyo for his valuable assistance.

Data availability

Data will be made available on request.

References

[1] G.M. Roba, et al., Making decisions without reliable information: the struggle of local traders in the pastoral meat supply chain, Food Policy 76 (2018) 33–43, https://doi.org/10.1016/j.foodpol.2018.01.013.
[2] Z. Alizadehsani, O. Hensel, A. Nasirahmadi, Multiscale transformer-based network for rangeland plant classification used in pasture scoring, Smart Agric. Technol. 12 (2025) 101183, https://doi.org/10.1016/j.atech.2025.101183.
[3] T.D. Hudson, et al., Big landscapes meet big data: informing grazing management in a variable and changing world, Rangelands 43 (1) (2020) 17–28, https://doi.org/10.1016/j.rala.2020.10.006.
[4] E. Mwangi, Property rights and governance of Africa's rangelands: a policy overview, Nat. Resour. Forum 33 (2009) 160–170.
[5] G.M. Roba, M.A. Lelea, B. Kaufmann, Manoeuvring through difficult terrain: how local traders link pastoralists to markets, J. Rural. Stud. 54 (2017) 85–97.
[6] F. D'Adamo, et al., Climatic and non-climatic vegetation cover changes in the rangelands of Africa, Glob. Planet. Change 202 (2021) 1–13, https://doi.org/10.1016/j.gloplacha.2021.103516.
[7] M. Mussa, H. Teka, Y. Mesfin, Land use/cover change analysis and local community perception towards land cover change in the lowland of Bale rangelands, Southeast Ethiopia, Int. J. Biodivers. Conserv. 9 (12) (2017) 363–372, https://doi.org/10.5897/IJBC2017.1131.
[8] M.E. Mgalula, et al., Mapping cropland evolution based on biophysical data and cropping history in the Borana rangelands, Southern Ethiopia, Reg Env. Change 23 (80) (2023) 1–11, https://doi.org/10.1007/s10113-023-02075-6.
[9] C. Munyati, Detecting the distribution of grass aboveground biomass on a rangeland using Sentinel-2 MSI vegetation indices, Adv. Space Res. 69 (2022) 1130–1145, https://doi.org/10.1016/j.asr.2021.10.048.
[10] E. Adam, N. Mureriwa, S. Newete, Mapping prosopis glandulosa (mesquite) in the semi-arid environment of South Africa using high-resolution WorldView-2 imagery and machine learning classifiers, J. Arid Env. 145 (2017) 43–51, https://doi.org/10.1016/j.jaridenv.2017.05.001.
[11] M. Elias, et al., Land conversion dynamics in the Borana rangelands of southern Ethiopia: an integrated assessment using remote sensing techniques and field survey data, Environments 2 (2015) 1–31, https://doi.org/10.3390/environments2010001.
[12] A. Retallack, et al., Remote sensing for monitoring rangeland condition: current status and development of methods, Environ. Sustain. Indic. 19 (2023) 100285, https://doi.org/10.1016/j.indic.2023.100285.
[13] Y. Alotaibi, et al., Optimal deep learning based vehicle detection and classification using chaotic equilibrium optimization algorithm in remote sensing imagery, Sci. Rep. 15 (2025) 17921, https://doi.org/10.1038/s41598-025-02491-0.
[14] M. Liu, et al., Zanthoxylum bungeanum maxim mapping with multi-temporal Sentinel-2 images: the importance of different features and consistency of results, ISPRS J. Photogramm. Remote Sens. 174 (2021) 68–86, https://doi.org/10.1016/j.isprsjprs.2021.02.003.
[15] E.C. Nnadozie, et al., Detecting Cassava plants under different field conditions using UAV-based RGB images and deep learning models, Remote Sens. (Basel) 15 (2023) 2322, https://doi.org/10.3390/rs15092322.
[16] V. De Cauwer, et al., A rangeland management-oriented approach to map dry savanna Woodland mosaics, Int. J. Appl. Earth Obs. Geoinf. 134 (2024) 104193, https://doi.org/10.1016/j.jag.2024.104193.
[17] V.E. Mtyobila, C. Shoko, Modelling lantana camara invasion in the inkomati catchment in Mpumalanga, South Africa, Phys. Chem. Earth 135 (2024) 103633, https://doi.org/10.1016/j.pce.2024.103633.

[18] W. Zewdie, E. Csaplovics, Identifying categorical land use transition and land degradation in northwestern drylands of Ethiopia, Remote Sens. (Basel) 8 (2016) 408, https://doi.org/10.3390/rs8050408.
[19] D. Gackstetter, K. Yu, M. Körner, Self-attention and frequency-augmentation for unsupervised domain adaptation in satellite image-based time series classification, ISPRS J. Photogramm. Remote Sens. 224 (2025) 113–132, https://doi.org/10.1016/j.isprsjprs.2025.03.024.
[20] L. Panda, et al., Methods of land cover classification using worldview-3 satellite images in land management, Tech. J. 18 (1) (2024) 142–147, https://doi.org/10.31803/tg-20221006135311.
[21] A.J. Rivera, et al., Analysis of clustering methods for crop type mapping using satellite imagery, Neurocomputing 492 (2022) (2022) 91–106, https://doi.org/10.1016/j.neucom.2022.04.002.
[22] T.T. Sankey, J.M. Leonard, M.M. Moore, Unmanned aerial vehicle-based rangeland monitoring: examining a century of vegetation changes, Rangel. Ecol. Manag. 72 (2019) 858–863, https://doi.org/10.1016/j.rama.2019.04.002.
[23] A. Patel, et al., Novel approach for the LULC change detection using GIS & Google Earth Engine through spatiotemporal analysis to evaluate the urbanization growth of Ahmedabad city, Results Eng. 21 (2024) 101788, https://doi.org/10.1016/j.rineng.2024.101788.
[24] Y. Zhen, et al., A clustering method for inter-annual NDVI time series, Remote Sens. Lett. 12 (8) (2021) 819–826, https://doi.org/10.1080/2150704X.2021.1941386.
[25] J.W. Rouse Jr., et al., Monitoring vegetation systems in the Great Plains with ERTS, NASA. Goddard Space Flight Cent. 3d ERTS-1 Symp. 1 (Sect. A) (1974) 309–317.
[26] G. Ballut-Dajud, et al., Diagnosis of the vegetation cover in the wetlands of La Caimanera Swamp, Colombia and Casitas Wetland, Mexico by means of Landsat and Sentinel-2A images during last four decades, Results Eng. 25 (2025) 104211, https://doi.org/10.1016/j.rineng.2025.104211.
[27] E. Sanz, et al., Clustering arid rangelands based on NDVI annual patterns and their persistence, Remote Sens. (Basel) 14 (2022) 4949, https://doi.org/10.3390/rs14194949.
[28] G. Chaturvedi, K. Avishek, Geospatial approach to identify the indicators of wetland change: a study for Kabartal (Ramsar Wetland), India, Results Eng. 24 (2024) 102999, https://doi.org/10.1016/j.rineng.2024.102999.
[29] S.V. Gaikwad, et al., Vegetation cover classification using Sentinal-2 time-series images and K-means clustering, in: 2021 IEEE Bombay Section Signature Conference (IBSSC), 2021, https://doi.org/10.1109/IBSSC53889.2021.9673181.
[30] N. Kuppala, K.C. Navneet, V.V. Sajith Variyar, R. Sivanpillai, Mapping vegetation dynamics in Wyoming: a multi-temporal analysis using Landsat NDVI and clustering, Int. Arch. Photogramm. Remote Sens. Spat. Inf. Sci (2024) 87–94, https://doi.org/10.5194/isprs-archives-XLVIII-M-5-2024-87-2025. XLVIII-M-5-2024.
[31] N. Siabi, S.H. Sanaeinejad, B. Ghahraman, Effective method for filling gaps in time series of environmental remote sensing data: an example on evapotranspiration and land surface temperature images, Comput. Electron. Agric. 193 (2022) 106619, https://doi.org/10.1016/j.compag.2021.106619.
[32] G. Zhang, X. Xiao, J. Dong, W. Kou, C. Jin, Y. Qin, Y. Zhou, J. Wang, M. A. Menarguez, C. Biradar, Mapping paddy rice planting areas through time series analysis of Modis land surface temperature and vegetation index data, ISPRS J. Photogramm. Remote Sens. 106 (2015) 157–171, https://doi.org/10.1016/j.isprsjprs.2015.05.011.
[33] A. Hippert-Ferrer, Y. Yan, P. Bolon, Em-EOF: gap-filling in incomplete SAR displacement time series, IEEE Trans.Geosci. Remote Sens. 59 (2020) 57945811, https://doi.org/10.1109/TGRS.2020.3015087.
[34] Y. Julien, J.A. Sobrino, Comparison of cloud-reconstruction methods for time series of composite NDVI data, Remote Sens Env. 114 (2010) 618–625, https://doi.org/10.1016/j.rse.2009.11.001.
[35] J. Mohite, S. Sawant, A. Pandit, S. Pappula, Investigating the performance of random forest and support vector regression for estimation of cloud-free ndvi using sentinel-1 sar data. the international archives of the photogrammetry, Remote Sens. Spat. Inf. Sci. 43 (2020) 1379–1383.
[36] M. Sun, A. Gong, X. Zhao, N. Liu, L. Si, S. Zhao, Reconstruction of a monthly 1 km ndvi time series product in china using random forest methodology, Remote Sens. (Basel) 15 (2023) 3353, https://doi.org/10.3390/rs15133353.
[37] A.V. Oppenheim, Discrete-time Signal Processing, Pearson Education India, 1999.
[38] J. Chen, P. Jönsson, M. Tamura, Z. Gu, B. Matsushita, L. Eklundh, A simple method for reconstructing a high-quality NDVI time-series data set based on the savitzky-golay filter, Remote Sens Env. 91 (2004) 332–344.
[39] J. Zhou, L. Jia, M. Menenti, Reconstruction of global Modis NDVI time series: performance of harmonic analysis of time series (HANTS), Remote Sens Env. 163 (2015) 217–228, https://doi.org/10.1016/j.rse.2015.03.01.
[40] D. Kong, Y. Zhang, X. Gu, D. Wang, A robust method for reconstructing global modis evi time series on the google earth engine, ISPRS J. Photogramm. Remote Sens. 155 (2019) 13–24, https://doi.org/10.1016/j.isprsjprs.2019.06.014.
[41] F. Sedano, P. Kempeneers, G. Hurtt, A kalman filter-based method to generate continuous time series of medium-resolution ndvi images, Remote Sens. (Basel) 6 (2014) 12381–12408, https://doi.org/10.3390/rs61212381.
[42] X. Lu, R. Liu, J. Liu, S. Liang, Removal of noise by wavelet method to generate high quality temporal data of terrestrial modis products, Photogramm. Eng. Remote Sens. 73 (2007) 1129–1139.
[43] H.R. Ghafarian Malamiri, I. Rousta, H. Olafsson, H. Zare, H. Zhang, Gap-filling of modis time series land surface temperature (lst) products using singular spectrum analysis (ssa), Atmos. (Basel) 9 (2018) 334.
[44] R.B. Cleveland, W.S. Cleveland, J.E. McRae, I. Terpenning, et al., Stl: a seasonal-trend decomposition, J. Off. Stat 6 (1990) 3–73.
[45] J. Verbesselt, R. Hyndman, A. Zeileis, D. Culvenor, Phenological change detection while accounting for abrupt and gradual trends in satellite image time series, Remote Sens. Env. 114 (2010) 2970–2980.
[46] S. Kandasamy, F. Baret, A. Verger, P. Neveux, M. Weiss, A comparison of methods for smoothing and gap filling time series of remote sensing observations–application to modis lai products, Biogeosciences. 10 (2013) 4055–4071.
[47] J. Serra, Image Analysis and Mathematical Morphology, 1, Academic Press, 1982.
[48] R.M. Coliban, M. Ivanovici, NDVI time series reconstruction using morphological filtering, Natl. Acad. Sci. Lett. (2025), https://doi.org/10.1007/s40009-025-01833-w.
[49] M. Mauerman, et al., The long-term impact of multi-season droughts on livestock holdings and pastoralist decision-making in Marsabit, Kenya. J. Arid Environ. 211 (2023), https://doi.org/10.1016/j.jaridenv.2022.104928.
[50] J.M.K. Ojango, A.W. Muigai, E.P. Oyieng, J. Gitau, J. Audho, J. Gachora, Developing Community-Based Breeding Programs to Improve Productivity of Sheep and Goats in Turkana, Isiolo and Marsabit counties of Kenya. ILRI Project Brief, ILRI, Nairobi, Kenya, 2021.
[51] S.R. Karlsen, et al., Time-series of cloud-free Sentinel-2 NDVI data used in mapping the onset of growth of central Spitsbergen, Svalbard. Remote Sens. 13 (2021) 3031, https://doi.org/10.3390/rs13153031.
[52] D. Dzulfansyah, et al., QField for QGIS application for oil palm agronomist's field visit and assessment, in: 7th International Oil Palm Conference, 2024.
[53] T. Kupach, et al., Software for field research: QField, XVII Int. Sci. Conf. "Monitoring Geol. Process. Ecol. Cond. Environ. (2023).
[54] O. Wasonga, et al., Vegetation Resources and Their Economic Importance in Isiolo County, Kenya, International Institute for Environment and Development (IIED), London, 2016. https://Pubs.Iied.Org/10141IIED.
[55] H.J. Heijmans, Composing morphological filters, IEEE Trans. Image Process. 6 (1997) 713–723.
[56] M. Yavari, P. Moallem, M. Kazemi, S. Moradi, Multi-stage morphological operators for small infrared target detection, Opt. (Stuttg) 276 (2023) 170597.
[57] P. Soille, et al., Morphological Image analysis: Principles and Applications, 2, Springer, 1999.
[58] Arthur, D., Vassilvitskii, S., 2006. k-means++: the advantages of careful seeding. Technical Report. Stanford.
[59] H.W. Kuhn, The hungarian method for the assignment problem, Nav. Res. Logist. (2) (1955) 83–97.
[60] M. Sokolova, G. Lapalme, A systematic analysis of performance measures for classification tasks, Inf. Process. Manage 45 (2009) 427–437.
[61] M. Abdulrazaq, Rare-event prediction in imbalanced data: a unified evaluation and optimization framework for high-risk systems, Commun. Phys. Sci. 9 (4) (2023) 968–979. Available at, https://journalcps.com/index.php/volumes/article/view/740.
[62] F. Evrendilek, O. Gulbeyaz, Deriving vegetation dynamics of natural terrestrial ecosystems from MODIS NDVI/EVI data over Turkey, Sensors 8 (2008) 5270–5302, https://doi.org/10.3390/s8095270.
[63] x. Huang, et al., A 10 m resolution land cover map of the Tibetan Plateau with detailed vegetation types, Earth Syst. Sci. Data 16 (2024) 3307–3332.